

Topological shape optimization of multifunctional tissue engineering scaffolds with level set method

Yu Wang¹ · Zhen Luo¹ · Nong Zhang¹ · Qinghua Qin²

Received: 9 December 2014 / Revised: 23 January 2016 / Accepted: 27 January 2016 / Published online: 4 March 2016
© Springer-Verlag Berlin Heidelberg 2016

Abstract A tissue engineering scaffold provides a proper environment to support physiological loads, and enhance cell migration and delivery for re-modeling of regenerating tissue. Hence, in the design of scaffolds, it is required to control the scaffold architecture with mechanical and mass transport properties simultaneously. In this paper, a level set-based topology optimization method will be developed to systematically generate three dimensional (3D) microstructures for tissue engineering scaffolds, with the prescribed properties for mechanical stiffness, fluid porosity and permeability. To create the internal architecture for scaffolds with desired properties, the numerical homogenization method will be used to evaluate the effective properties of the microstructure for building the periodic composite media, and a parametric level set method will be introduced to find the optimized shape and topology of the microstructure. Several numerical examples are used to demonstrate the effectiveness of the proposed method in achieving scaffolds with desired multifunctional properties, within the numerically estimated cross-property

bounds between the effective bulk modulus and permeability under different porosities.

Keywords Tissue scaffolds · Microstructure · Topology optimization · Level set method

1 Introduction

In the early 1990s, tissue engineering was mainly developed to overcome the limitations of tissue graft and alloplastic repair (Lanza 2011). The fundamental essence of tissue engineering is to adapt a porous degradable material called scaffold to transplant bio-factors like stem-cell and gene-therapy approaches, which is used to stimulate tissue repair. Hence, the design of porous biomaterials, such as the scaffold architecture, plays an important role in the tissue regeneration. A basic tissue engineering design hypothesis is that the scaffold should provide a biomimetic mechanical environment for initial function and sufficient porosity for cell migration and cell/gene delivery (Hollister 2005; Hollister et al. 2002). To fulfill such multifunctional design requirements, there are several functional characteristics to be considered, such as the porosity, mechanical modulus and permeability/diffusivity. For example, bone tissue engineering scaffolds should be designed to have high diffusivity, permeability or porosity for better cell migration and biologics transport to meet the multi-criteria requirements (Kang et al. 2010). Furthermore, the multifunctional characteristics often vary with the specific tissue. For instance, to maintain the health of bone tissues, taking the trabecular bone as an example, the elastic modulus has a wide range from 10 to 1500 MPa (Goulet et al. 1994). While, the aggregate modulus for articular cartilages is relatively smaller with a range from 0.5 to 3.0 MPa (Boschetti et al. 2004), comparing to that of trabecular bones. Thus, the design

This paper is submitted for possible publication in *Structural and Multidisciplinary Optimization*. It has not been previously published, is not currently submitted for review to any other journals, and will not be submitted elsewhere during the peer review. It is noted that this manuscript has been submitted in a style of “*Your Paper Your Way*” only for the convenience of peer-review.

✉ Zhen Luo
zhen.luo@uts.edu.au

¹ School of Electrical, Mechanical and Mechatronic Systems, The University of Technology, Sydney, NSW 2007, Australia

² Research School of Engineering, Australian National University, Canberra, ACT 2601, Australia

challenge of bone tissue engineering scaffolds is actually to explore suitable internal architecture to satisfy their multifunctional properties.

The multifunctional tissue scaffolds are attracting more and more attention in the field of bioengineering, and a number of different design methods (Hollister 2005; Hollister et al. 2002) have been developed to create scaffolds over the past. More recently, with the rapid development of computational design engineering, topology optimization technique has shown its potential as a powerful design tool for micro-structured scaffolds. Topology optimization (Bendsøe and Sigmund 2003) is a numerical process to iteratively redistribute a given amount of material to extremize a prescribed objective function under specific constraints, until the best material layout is achieved within a fixed reference domain. Several methods have been developed for topology optimization of structures, such as the homogenization method (Bendsøe and Kikuchi 1988), the SIMP method (Zhou and Rozvany 1991; Bendsøe and Sigmund 1999), ESO (Xie and Steven 1993) and the level set-based method (LSM) (Sethian and Wiegmann 2000; Wang et al. 2003; Allaire et al. 2004; Luo et al. 2008). Topology optimization has been applied to design scaffolds to topologically achieve the optimized layout of the micro-structure. For instance, Lin and et al. (Lin et al. 2004) applied the homogenization-based topology optimization method to design 3D internal scaffold architectures, to simultaneously meet the desired elastic properties and porosity for mass transport. Guest and Prevost (Guest and Prévost 2006) extended the projection method (Guest et al. 2004) to topological design of 3D scaffolds, to maximize the bulk modulus and isotropic permeability. Kruijff et al. (de Kruijff et al. 2007) used topology optimization to generate optimized scaffold structures having maximized bulk modulus and thermal conductivity in two-dimensional (2D) structures based on the Pareto optimality. Challis and et al. (Challis et al. 2008) developed a level set method to design microstructures with isotropic materials to gain maximized bulk modulus and isotropic conductivity. Challis and et al. (Challis et al. 2012) also proposed a method for the generation of numerically estimated cross-property bounds for stiffness and fluid permeability porous materials with level sets. Kang (Kang et al. 2010) applied the homogenization topology optimization to create 3D scaffold architectures, so as to match the desired elastic properties and porosity simultaneously. It is noted that the most of the above topology optimization methods are based on material density distribution.

Recently, the LSMs have been emerged as a new family of alternative approached for shape and topology optimization of structures. LSMs were originally developed for tracking, modelling and simulating shape variation of the moving boundary with topological changes by merging and breaking the boundary. LSMs have shown some unique characteristics as a result of the implicit free boundary representation, such as

(1) smooth boundary and distinct interface in the process of the optimization, (2) shape fidelity and topological flexibility, and (3) topological changes during shape variations (Wang et al. 2003; Allaire et al. 2004; van Dijk et al. 2013). However, in conventional LSMs the solution of the Hamilton-Jacobi partial differential equations (H-J PDE) using the finite difference method involves several numerical issues to be carefully handled (Osher and Sethian 1988; Sethian 1999; Osher and Fedkiw 2002), such as the re-initialization of the level set function (LSF), the Courant-Friedrichs-Lewy (CFL) condition, as well as the extension of the normal velocity. Hence, to overcome the unfavourable numerical features, several alternative LSMs have been developed more recently (van Dijk et al. 2013), e.g. the parametric level set method (PLSM) (Luo et al. 2008), which have been successfully applied to topological shape design of structures (Luo et al. 2012a; Wang et al. 2015), mechanisms (Luo et al. 2012b) and metamaterials (Wang et al. 2014). In PLSM, the key concept is to interpolate the original LSF using a set of compactly supported radial basis function (CS-RBF) (Wendland 2006) to ensure a desirable smoothness and accuracy of the approximation. In this way, the original H-J PDE is changed into a system of equations, and the topological shape optimization is converted to a size optimization, in which the expansion coefficients of the interpolant, which are temporal only, are considered as the design variables. Thus, many more efficient gradient-based optimization algorithms can be directly applied to the optimization problem.

However, the current paper is the first time the original parametric level set method (Luo et al. 2008) has been extended to a family of more advanced topology optimization problems in a different area of application, namely, topological shape design of three-dimensional (3D) Scaffold microstructures in tissue engineering. In this method, the numerical homogenization method will be used to evaluate the effective property, while the PLSM will be applied to optimize shape and topology of the microstructure by satisfying the prescribed properties, such as mechanical stiffness, fluid porosity and permeability. Several numerical examples are applied to demonstrate the effectiveness of the proposed method in optimizing the 3D tissue engineering scaffolds.

2 Homogenization of elasticity and permeability

In this study, we have the following assumptions: the composite only consists of arrays of periodically arranged microstructures or unit cells; the geometric size of the unit cell is much smaller than the macroscopic material to enable the scale-decomposition in the homogenization; the homogenized effective properties of the composite can be predicted by the mechanical

behaviour of the microstructure. Based on the small parameter perturbation of the displacement, the effective properties of the micro-structured scaffold architecture can be computed by using the numerical homogenization method (Guedes and Kikuchi 1990).

The effective elasticity tensor \mathbf{C}^H relates the macroscopic stress tensor $\boldsymbol{\sigma}$ to the macroscopic strain tensor $\boldsymbol{\varepsilon}$ for the porous biomaterials as follows:

$$\boldsymbol{\sigma} = \mathbf{C}^H \boldsymbol{\varepsilon} \quad (1)$$

where \mathbf{C}_{ijkl}^H is the effective stiffness tensor, given by

$$\mathbf{C}_{ijkl}^H = \frac{1}{|Y|} \int_Y \left(\varepsilon_{pq}^{0(ij)} - \varepsilon_{pq}^{*(ij)} \right) C_{pqrs} \left(\varepsilon_{rs}^{0(kl)} - \varepsilon_{rs}^{*(kl)} \right) dY \quad (2)$$

and ε^0 is the unit test strain field, $|Y|$ is the volume of the cell, and ε^* is the strains tensor corresponding to the displacement field χ^{kl}

$$\varepsilon_{pq}^{*(kl)} = \frac{1}{2} \left(\frac{\partial \chi_p^{kl}}{\partial y_q} + \frac{\partial \chi_q^{kl}}{\partial y_p} \right) \quad (3)$$

Here χ^{kl} can be obtained by solving the following equation: Find $\chi^{kl} \in U_{period}(Y)$ such that

$$\int_Y C_{ijpq} \frac{\partial \chi_p^{kl}}{\partial y_q} \frac{\partial v_i}{\partial y_j} dY = \int_Y C_{ijpq} \frac{\partial v_i}{\partial y_j} dY \quad \forall v \in U_{period}(Y) \quad (4)$$

where ν is the virtual displacement field, $U_{period}(Y)$ is the kinematically admissible displacement space with Y -period. Since the 3D biomaterial with cubic elastic symmetry is considered in this study, this material has an effective stiffness matrix with three independent components of the form

$$\mathbf{C}^H = \begin{bmatrix} C_{11}^H & C_{12}^H & C_{12}^H & 0 & 0 & 0 \\ C_{12}^H & C_{11}^H & C_{12}^H & 0 & 0 & 0 \\ C_{12}^H & C_{12}^H & C_{11}^H & 0 & 0 & 0 \\ 0 & 0 & 0 & C_{44}^H & 0 & 0 \\ 0 & 0 & 0 & 0 & C_{44}^H & 0 \\ 0 & 0 & 0 & 0 & 0 & C_{44}^H \end{bmatrix} \quad (5)$$

The bulk modulus is a commonly used stiffness measure in topology optimization to study the resistance of the material to a volumetric strain. The effective bulk modulus B^H for a material with cubic elastic symmetry is

$$B^H = \frac{1}{3} C_{11}^H + \frac{2}{3} C_{12}^H \quad (6)$$

The permeability for slowly moving incompressible fluids within porous materials can be simulated using the

homogenization of Stokes flows through a porous material with Darcy's law on the macroscopic scale

$$\mathbf{U} = -\frac{1}{\mu} \mathbf{K}^H \nabla P \quad (7)$$

where \mathbf{U} is the average fluid velocity, ∇P is the pressure gradient across a porous material, \mathbf{K}^H is the effective fluid permeability tensor and μ is the viscosity of the fluid. In this study, the numerical homogenization method for the fluid follows the method given by Guest and Prévost (Guest and Prévost 2006). By applying the stabilization technique (Hughes et al. 1986) for the Stokes flow and Darcy flow, the effective permeability tensor can be computed as

$$\mathbf{K}^H = [\mathbf{K}_{ij}^H] = \frac{1}{|Y|} \mathbf{w}^{(i)T} \mathbf{K}_{ds} \mathbf{w}^{(j)} \quad (8)$$

where \mathbf{K}^H is the effective fluid permeability, \mathbf{K}_{ds} is Darcy-Stokes viscosity matrix. $\mathbf{w}^{(i)}$ is the velocity vector which can be solved numerically using the stabilized finite element to avoid the Babuska -Brezzi condition (Guest and Prévost 2006).

A material with the isotropic flow symmetry has an isotropic effective permeability matrix, which is:

$$\mathbf{K}^H = \begin{bmatrix} K_{11}^H & 0 & 0 \\ 0 & K_{11}^H & 0 \\ 0 & 0 & K_{11}^H \end{bmatrix} \quad (9)$$

The scalar permeability can be computed as follows:

$$k^H = \frac{1}{d} \sum_{i=1}^d K_{ii}^H \quad (10)$$

where d is the dimension and equals to three for 3D problems.

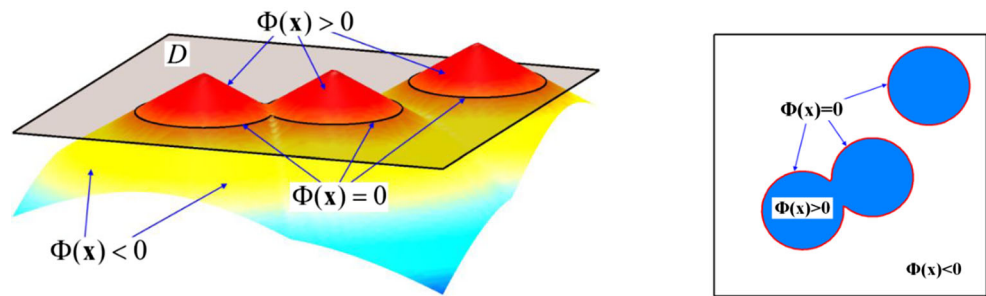
3 Parametric level set method

In level set method, the design boundary is implicitly represented as the zero level set of a higher-dimensional level set function (LSF) $\Phi(\mathbf{x})$ (Osher and Sethian 1988; Sethian 1999; Osher and Fedkiw 2002), which is defined over a reference domain $D \subset \mathbb{R}^d$ ($d=2$ or 3). Figure 1 shows a 2D design boundary represented by a 3D level set surface. The 2D boundary is embedded as follows:

$$\begin{cases} \Phi(\mathbf{x}) > 0 & \forall \mathbf{x} \in \Omega \setminus \partial\Omega & \text{(Solid region)} \\ \Phi(\mathbf{x}) = 0 & \forall \mathbf{x} \in \partial\Omega \cap D & \text{(Design boundary)} \\ \Phi(\mathbf{x}) < 0 & \forall \mathbf{x} \in D \setminus \Omega & \text{(Void region)} \end{cases} \quad (11)$$

To enable the dynamic motion, the pseudo-time t is introduced into the LSF $\Phi(\mathbf{x})$, which leads to the

Fig. 1 (Left) 3D level set function; (Right) Design domain at the zero level set



following first-order H-J PDE by differentiating $\Phi(\mathbf{x}, t) = 0$ on both sides with respect to t :

$$\frac{\partial \Phi(\mathbf{x}, t)}{\partial t} + \mathbf{v} \cdot |\nabla \Phi(\mathbf{x}, t)| = 0 \quad (12)$$

where $\mathbf{v} = d\mathbf{x}/dt$ is the velocity field at the design boundary. Only the normal velocity component v_n contributes to the shape evolution of the boundary (Wang et al. 2003; Allaire et al. 2004), which is expressed as follows:

$$v_n = \mathbf{v} \cdot \mathbf{n} = \mathbf{v} \cdot \left(-\frac{\nabla \Phi}{|\nabla \Phi|} \right) = \frac{d\mathbf{x}}{dt} \cdot \left(-\frac{\nabla \Phi}{\sqrt{\nabla \Phi \cdot \nabla \Phi}} \right) \quad (13)$$

The PLSM (Luo et al. 2008) has a parameterized level set surface via the interpolation of a given set of CS-RBFs positioned at given knots in the design space, in which the LSF can be expressed as follows:

$$\Phi(\mathbf{x}, t) = \varphi(\mathbf{x}) \alpha(t) = \sum_{i=1}^N \varphi_i(\mathbf{x}) \alpha_i(t) \quad (14)$$

where the vector of the shape functions (CS-RBF) is defined by

$$\varphi(\mathbf{x}) = [\varphi_1(\mathbf{x}), \varphi_2(\mathbf{x}), \dots, \varphi_N(\mathbf{x})] \in \mathbb{R}^N \quad (15)$$

and the expansion coefficient vector is

$$\alpha(t) = [\alpha_1(t), \alpha_2(t), \dots, \alpha_N(t)]^T \in \mathbb{R}^N \quad (16)$$

where N is the total number of the knots in the design domain.

It can be found that in the parametric level set method, the “parametric” denotes the sampling/interpolation of the original level set function, using the CS-RBF basis functions and the corresponding expansion coefficients at a set of scattered knots or points over the design domain.

The CS-RBFs (Wendland 2006) possess desirable properties in interpolation, including positive

definiteness and sparseness of the interpolation matrices under certain conditions, as well as the desired smoothness and continuity of the interpolant. In this work, we will use the following CS-RBF with C2 smoothness (Fig. 2).

$$\varphi_i(r) = \max\{0, (1-r^4)\}(4r+1) \quad (i = 1, 2, \dots, N) \quad (\text{Wendland-C2}) \quad (17)$$

The above interpolation leads to a separation scheme of the space and time, in which the shape functions are spatial only and the generalized expansion coefficients are time dependent only. The decoupling of the time and space terms of the H-J PDE results in

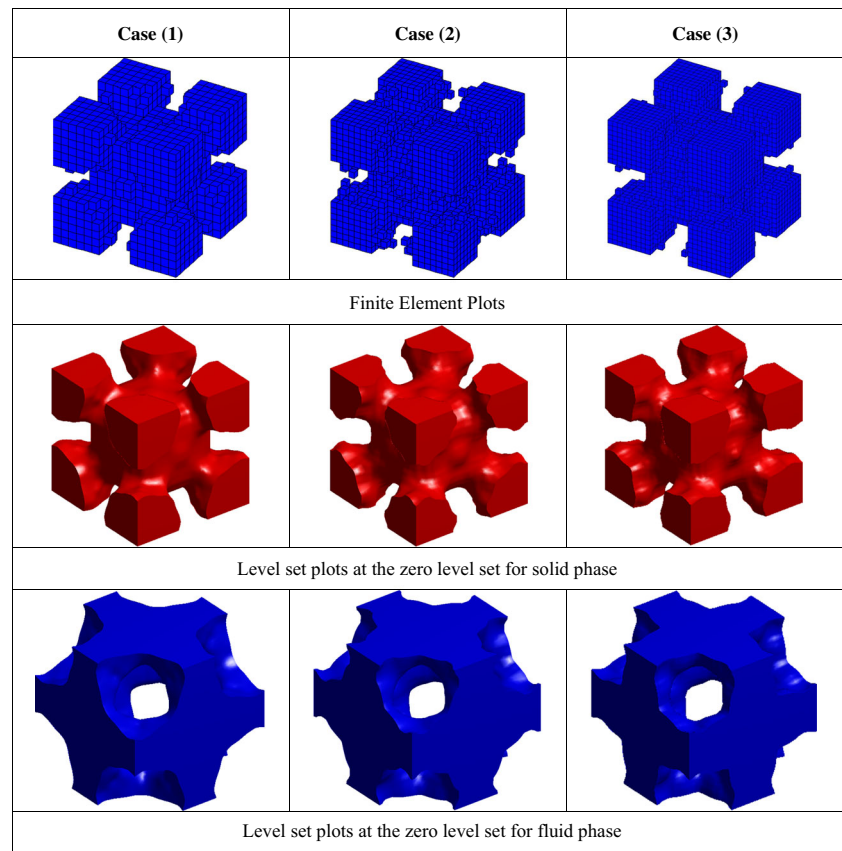
$$\varphi(\mathbf{x}) \frac{\partial \alpha(t)}{\partial t} - v_n |\nabla \varphi(\mathbf{x}) \alpha(t)| = 0 \quad (18)$$

Thus the normal velocity v_n is related to the time derivative of the expansion coefficients $\alpha(t)$ as follows:

$$v_n = \frac{\varphi(\mathbf{x})}{|\nabla \varphi(\mathbf{x}) \alpha(t)|} \frac{\partial \alpha(t)}{\partial t} \quad (19)$$

We can find that all the terms involved in v_n are actually evaluated at all the knots in the design domain, and v_n is actually extended to the whole design domain. In this way, the H-J PDE has been parameterized into a system of equations only with a set of unknowns $\alpha(t)$, which act as the design variables. The propagation of the LSF is just a matter of finding $\alpha(t)$ with an appropriate optimization algorithm. It is noted that there are normally two sets of meshes are involved in level-set based topology optimization methods. The first is to calculate the field quantities (e.g. displacements and strains), and the second is used for propagation of the level set surface.

Fig. 2 Optimization results for porosity 50 % under different mesh level



With the parameterization, the original H-J PDE actually becomes a system of ODEs in which the expansion coefficients are temporal only. However, in the practical numerical implementation, the design variables will be updated sequentially and iteratively using an appropriate optimization algorithm. In this case, from the point of view of iterative optimization, the topological shape optimization problem is essentially changed into a generalized “size” optimization. Here, the “size” refers to the expansion coefficients to be updated under a convergence criterion. In this case, we may say that the “size” optimization problem is similar to SIMP, as the update of the expansion coefficients over the knots is similar to the update of elemental densities in the SIMP.

4 Multi-objective optimization problem

Tissue engineering scaffolds are a family of porous biomaterials designed to mainly both bear mechanical loading and enable mass transport. The design of such multifunctional composite materials is actually the multi-objective topology optimization problem.

4.1 Material description model using level sets

At an arbitrary point x , the elasticity tensor of the practical material can be given by

$$\mathbf{C}(x) = \mathbf{C}_{\text{base}} H(\Phi(x)) \quad (20)$$

where \mathbf{C}_{base} is the elasticity tensor of the solid material, and H is the Heaviside function, often given as follows:

$$H(\Phi(x)) = \begin{cases} \frac{3(1-\theta)}{4} \left(\frac{\Phi(x)}{\Delta} - \frac{\Phi(x)^3}{3\Delta^3} \right) + \frac{1+\theta}{2} & -\Delta \leq \Phi(x) < \Delta \\ 1 & \Phi(x) \geq \Delta \\ 0 & \Phi(x) < -\Delta \end{cases} \quad (21)$$

where θ is a small positive number (e.g. $1e-4$) to ensure the non-singularity of element stiffness matrix, and Δ is the width for the numerical approximation of the Heaviside function. In the numerical implementation, the Heaviside function is usually smoothed to facilitate the calculation of the first-order derivatives.

For the permeability, the interpolation of the Darcy-Stokes viscosity matrix \mathbf{K}_{ds} is given by

$$\mathbf{K}_{\text{ds}}(x) = \mathbf{K}_{\text{d}} H(\Phi(x)) + \mathbf{K}_{\text{s}} [1 - H(\Phi(x))] \quad (22)$$

where \mathbf{K}_{d} is Darcy stiffness tensor and \mathbf{K}_{s} is Stokes stiffness

tensor. The above equation denotes that the flow through the solid phase is governed by Darcy's law, while the fluid phase is treated as Stokes flow. Assuming that the design domain with volume $|Y|$, the porosity of material can be calculated as

$$V = 1 - \frac{1}{|Y|} \int_Y H(\Phi(\mathbf{x})) dY \quad (23)$$

4.2 Formulation of the optimization problem using PLSM

In order to achieve the prescribed material properties, the optimization problem is defined as a weighted multi-objective formulation to minimize the error between the prescribed values and the effective values of the bulk modulus and permeability simultaneously, subject to constraints on porosity and symmetric conditions.

$$\begin{cases} \text{Find } \alpha \\ \text{minimize } J = \omega_B (B^H(\alpha) - B^*)^2 + \omega_k (k^H(\alpha) - k^*)^2 \\ \text{subject to } \mathbf{V}(\alpha) = \mathbf{V}^* \\ \mathbf{g}(\mathbf{C}^H(\alpha), \mathbf{K}^H(\alpha)) \leq 0 \\ \mathbf{h}(\alpha) = 0 \end{cases} \quad (24)$$

Here α is the vector of design variables, B^* and k^* correspond to the prescribed bulk modulus and permeability of the microstructure, \mathbf{V}^* is the required porosity of the material, and $\mathbf{V}(\alpha)$ is the practical porosity of the material. In the numerical implementation, the equality

constraint of the porosity can be achieved with a tolerance of 1 %. The equality constraint $\mathbf{h}(\alpha) = 0$ represent the equilibrium equations. The inequalities $\mathbf{g}(B^H(\alpha), k^H(\alpha)) \leq 0$ represent the constraints on the effective constitutive tensors, including symmetry constraints. We will consider cubic symmetry for the elastic properties and isotropic symmetry for the flow in the study. ω_B and ω_k are weighting factors used to indicate the relative importance of the two objectives in the design.

In PLSM, the Hamilton-Jacobi PDE driven topological optimization problem has been transformed into a standard parametric optimization problem with a set of generalized "sizes" as the design variables. Actually, the "size" refer to the set of expansion coefficients related to the CS-RBF interpolation. In this case, we do not need to explicitly calculate the normal velocity field \mathbf{v}_n on the level-set boundary and extend the normal velocity field from the boundary to the design domain. However, we still need the expression of the normal velocity field \mathbf{v}_n after the parameterization, because this normal velocity field \mathbf{v}_n will be subsequently used to help derive the design sensitivity together with the shape derivative analysis method and the chain rule.

The derivatives of the \mathbf{C}_{ijkl}^H with respect to t is expressed as

$$\frac{d\mathbf{C}_{ijkl}^H}{dt} = \frac{1}{|Y|} \int_Y \left(\varepsilon_{pq}^{0(ij)} - \varepsilon_{pq}^*(\chi^{ij}) \right) C_{pqrs} \left(\varepsilon_{rs}^{0(kl)} - \varepsilon_{rs}^*(\chi^{kl}) \right) \delta(\Phi) \mathbf{v}_n |\nabla \Phi| dY \quad (25)$$

where $\delta(\Phi)$ is the Dirac function, which is the first-order derivative of the Heaviside function $H(\Phi)$.

Subjecting \mathbf{v}_n expressed by Eqs. (19) to (25) leads to

$$\frac{d\mathbf{C}_{ijkl}^H}{dt} = \left(\frac{1}{|Y|} \int_Y \left(\varepsilon_{pq}^{0(ij)} - \varepsilon_{pq}^*(\chi^{ij}) \right) C_{pqrs} \left(\varepsilon_{rs}^{0(kl)} - \varepsilon_{rs}^*(\chi^{kl}) \right) \delta(\Phi) \varphi_i(\mathbf{x}) dY \right) \frac{\partial \alpha_i(t)}{\partial t} \quad (26)$$

At the same time, the derivative of \mathbf{C}_{ijkl}^H with respect to t can be given as follows by using the chain rule

$$\frac{d\mathbf{C}_{ijkl}^H}{dt} = \frac{\partial \mathbf{C}_{ijkl}^H}{\partial \alpha_i(t)} \frac{\partial \alpha_i(t)}{\partial t} \quad (27)$$

Comparing the corresponding terms of Eqs. (26) and (27), we can find the sensitivities of \mathbf{C}_{ijkl}^H with respect to the design variables α_i by

$$\frac{d\mathbf{C}_{ijkl}^H}{d\alpha_i} = \frac{1}{|Y|} \int_Y \left(\varepsilon_{pq}^{0(ij)} - \varepsilon_{pq}^*(\chi^{ij}) \right) C_{pqrs} \left(\varepsilon_{rs}^{0(kl)} - \varepsilon_{rs}^*(\chi^{kl}) \right) \delta(\Phi) \varphi_i(\mathbf{x}) dY \quad (28)$$

($i = 1, 2, \dots, N$)

Similarly, the sensitivity of \mathbf{K}_{kl}^H with respect to the design variables α_i is

$$\frac{d\mathbf{K}_{kl}^H}{d\alpha_i} = \frac{1}{|Y|} \int_Y \mathbf{w}^{(i)\top} (\delta(\Phi) \mathbf{K}_d - \delta(\Phi) \mathbf{K}_s) \mathbf{w}^{(j)} \varphi_i(\mathbf{x}) dY \quad (i = 1, 2, \dots, N) \quad (29)$$

The sensitivity of the volume constraint (porosity) is given as

$$\frac{dV}{d\alpha_i} = -\frac{1}{|Y|} \int_Y \delta(\Phi) \varphi_i(\mathbf{x}) dY \quad (i = 1, 2, \dots, N) \quad (30)$$

Once the sensitivity information has been obtained, many more efficient optimization algorithms like MMA (Svanberg

1987) can be applied to update the design variables (expansion coefficients of the CS-RBF interpolation) iteratively. Then, the interpolant of the level set function will be updated correspondingly, which will lead to the motion of the level set boundary as well as the evolution of the shape and topology of the structure.

4.3 Numerical implementation of the topology optimization problem

In the numerical implementation, the “artificial” material model will be used for the solid phase and the periodic boundary condition will be applied to the design domain of the unit cell (microstructure). Geometrical symmetries of the unit cell are considered to achieve cubic elastic symmetric material phase and isotropic flow phase. The standard finite element method (FEM) is employed to discretize the unit cell in order to obtain the displacement field. In this study, the eight-node isoparametric elements will be used to discretize the design domain.

In the conventional SIMP approach, element-wise density variables are usually regarded as the design variables. In order to overcome the typical numerical difficulties (e.g. checkerboards), many attempts have been made to formulate the topology optimization problems based on point-wise design variables to evaluate material properties at nodes or meshless points, e.g. (Guest et al. 2004; Luo et al. 2012a; Kang and Wang 2011; Luo et al. 2013). In this study, the material properties are also evaluated at nodes as nodal values. Thus, the LSF is sampled and determined by the interpolation using the CS-RBFs at these nodal positions for the simplicity, as given in Eq. (14). It should be noted that the CS-RBFs knots are not necessarily required to be at the same positions as the element nodes.

In the level set-based methods, when the boundary crosses an element, it is usually difficult to accurately calculate strain and stiffness of the element. To resolve this problem, there have been several methods available, such as, the widely used “ersatz” model (Allaire et al. 2004). In this study, an alternative scheme numerically more accurate is applied to evaluate the strain field, based on the computational points ($3 \times 3 \times 3$ Gauss points) of the element. It is a FEM-based alternative scheme, which fully takes advantage of the concept of compactly supported influence domain, e.g. (Kang and Wang 2011; Luo et al. 2013). The material property for each Gaussian point is evaluated by using the interpolation of CS-RBFs and material properties at those nodes located within a compact support domain. The Gaussian points are used as computational points to approximate strain and stiffness of those 3D finite elements cut by the boundary.

Then, in the numerical process, the material properties of the Gauss points are determined by the values of the smoothed Heaviside function $H(\Phi)$, which are subsequently applied to

assemble the stiffness and Darcy-Stokes viscosity matrices by Eqs. (20) and (22). Namely, the material is assigned to be void/fluid when $H(\Phi)$ takes a small value $\theta = 1e-4$ (the elasticity tensor \mathbf{C} is close to zero, and the Darcy-Stokes viscosity matrix \mathbf{K}_{ds} equals to Stokes stiffness tensor \mathbf{K}_s), and solid when $H(\Phi)$ equals to 1. When $H(\Phi)$ is between $1e-4$ and 1, properties \mathbf{C} and \mathbf{K}_{ds} can be determined according to the interpolation scheme, given in Eqs. (20) and (22), respectively.

The equilibrium equations for the homogenization problem are solved using the FEM to calculate the effective material properties. In the PLSM, the propagation of the LSF is driven by updating the design variables using the Method of Moving Asymptotes (MMA) (Svanberg 1987). To use the gradient-based MMA optimizer, it is necessary to calculate the design sensitivity. The design is iteratively optimized until the change of two successive objective function values is less than 0.001, or a maximum of 200 iterations is reached in terms of numerical experience. Compared with the conventional LSMs, in PLSM no re-initialization is required. Moreover, this method is free from the CFL condition, as the topological shape changes is driven by updating the design variables with the MMA, rather than by numerically solving the Hamilton-Jacobi PDE.

5 Numerical examples

In this section, several numerical examples are used to demonstrate the effectiveness of the proposed approach in designing the scaffold architecture with the prescribed stiffness and mass transport properties. The artificial material is supposed to have Young’s modulus $E=1$ and Poisson’s ratio $\nu=0.3$. The goal of the design is to achieve target design points with specified effective bulk modulus and permeability within the numerically estimated cross-property upper bounds (Challis et al. 2012). The radius of CS-RBF is set to be 2.5 times of the average CS-RBF knots distance (set to be 1) in this study. Different finite element meshes and different porosities will be used to investigate the effectiveness of the proposed optimization method.

5.1 Design with different meshes

In this section, the microstructure, with the porosity 50 %, the prescribed bulk modulus 0.22 and permeability 0.0005, is optimized under different meshes, e.g. $15 \times 15 \times 15 = 3375$, $20 \times 20 \times 20 = 8000$ and $25 \times 25 \times 25 = 15625$. The optimization parameters and the properties of the microstructure are given in Table 1, and the final results are shown in Fig. 2, where the “Finite Element Plots” are actually elemental stiffness plots. More details about this case can be found in Case (f) given in Section (3). The effective element stiffness can be computed based on the properties evaluated at the Gauss

Table 1 Optimization parameters and properties of designed microstructures

Case	Meshes	Elements	Computational points	Iterations	Achieved porosity	Achieved bulk modulus	Achieved permeability
(1)	$15 \times 15 \times 15$	3,375	91,125	136	50.7545 %	0.2167	0.000505
(2)	$20 \times 20 \times 20$	8,000	216,000	199	50.7275 %	0.2168	0.000506
(3)	$25 \times 25 \times 25$	15,625	421,875	195	50 %	0.2168	0.000505

points of the element. Elements are plotted when the value of stiffness is larger than a given threshold value (e.g. $0.5 \cdot C_{\text{base}}$). It is straightforward to plot the element stiffness. From the finite element plots of the design, it can be found that the optimized topologies are almost the same under the different meshes. Furthermore, with the increase of the number of finite elements, the effective properties of the topologically optimized microstructures change slightly, but more iterations and longer computational time are required for the design to converge.

Based on the final topology at the zero level set, we can find that the boundary of the material phase is smooth and the material interface is distinct. For most numerical approximation methods a finer mesh may be more suitable for a better description of the boundary condition and a better approximation of the field quantities. Hence, a higher meshing resolution may benefit the topological shape description and numerical accuracy, but the computational cost will increase. Here, the mesh size is determined based on our numerical experience.

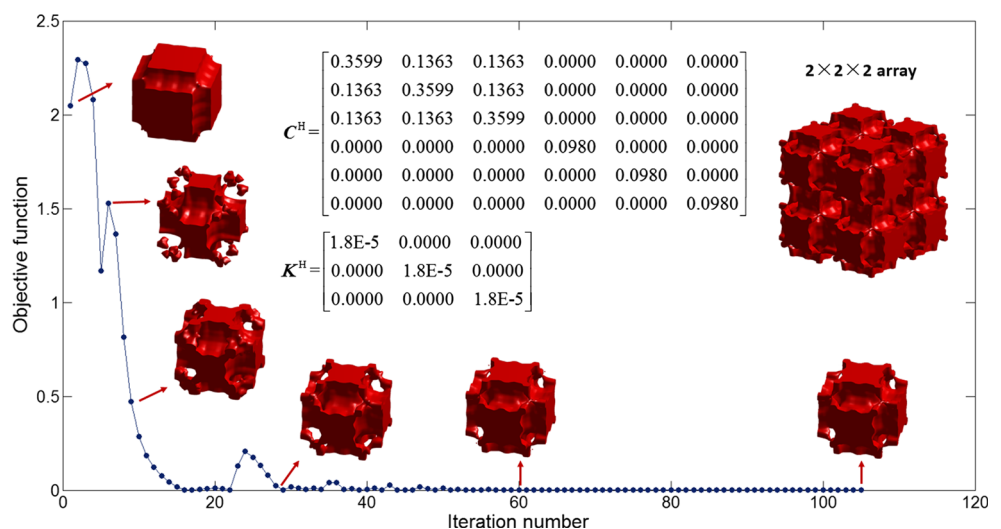
5.2 Convergence of the design

The convergence history given in Fig. 3 shows a case with the same initial design as that of Cases (a) and (h) in next Section. However, the objective of this design is to achieve an effective bulk modulus 0.2 and permeability $2\text{E-}5$ under the porosity 50 %. After 105 iterations, this optimization process

converges at a high effective bulk modulus 0.1981 and a very low permeability $1.8\text{E-}5$. Although the nucleation mechanism of new holes in 2D design problem is important, but in 3D designs such mechanism is less important because new holes can be developed by pinching two boundaries (occur without destroying the connectivity of the structure).

As shown in Fig. 3, it can be found that the level set method (Sethian and Wiegmann 2000; Wang et al. 2003; Allaire et al. 2004; Luo et al. 2008; van Dijk et al. 2013) has unique features which make the designs including intermediate designs have explicitly trackable smooth boundaries and geometrical-ly distinct interface. Furthermore, we can see that the proposed approach is able to integrate shape optimization and topology optimization as a seamless procedure of topological shape optimization. It is easy to find that the evolution of the topology is completed within the first 40 iterations, and the rest around 80 iterations are mainly used to complete shape variations. Compared with the conventional LSMs (e.g. (Allaire et al. 2004)), the proposed method has been proven to be more efficient and it can find the optimized design normally within 150 iterations.

Here it is noted that the iteration numbers for a level set-based topology optimization actually depend on the applied formulation: (1) If the standard level set method (Wang et al. 2003; Allaire et al. 2004) is used, the iteration for the convergence may be over 1000 iterations or even more, due to the time step limitation of the CFL condition; (2) When the

Fig. 3 Convergence of the objective function

discrete level set method, e.g. (Challis 2010), is used, the iteration for a general convergence criterion will be from 100 to 200 iterations; (3) For the parametric level set method (Luo et al. 2008), 200–300 iterations will be normally required for convergence, due to the removal of the time-step limitation of the CFL condition.

Actually, we can flexibly select initial designs for topology optimization problems of structures. It is well known that the same initial structures may lead to different designs if they have been given different objective functions and constraints. Alternatively, different initial structures may generate the same designs for the same optimization problem. In this study, we can find that in some situations the same initial designs can produce the different designs, and sometimes the different designs can lead to different optimized designs, which is further showcase the flexibility on the selection of initial designs for the optimization. Having regard to the design of microstructures, in terms of our numerical experience, we should address that the initial design domain had better involve inhomogeneity of material, so as to facilitate the numerical homogenization method more effectively in estimating the effective properties of the microstructure. It is noted that the locations, shapes and numbers of holes may all have the influence for the approximation of the numerical homogenization method, and as a result effect the optimized designs.

Meanwhile, if an initial design is happened to satisfy the volume constraint, it may enhance the stability of the optimization process and reduce the total numbers of iterations for convergence. It can be found that the different initial microstructures can give different microstructural architecture designs, although the effective properties of the designs may be similar (Guedes et al. 2003). This phenomenon should be because of multiple local solutions due to non-convexity of the topology optimization problem with the homogenized composite material. Another reason is that for the macro structure consisting of arrays of periodic micro unit cells, each unit cell has periodic boundary condition. The microstructural pattern for repeatedly assembling the macro structure is not unique, depending on how to identify and extract the unit cell from the periodic material, which is found in (Lin et al. 2004) as well.

5.3 Designs with different porosities

In this section, we will design microstructures to have a range of effective bulk moduli and permeability values with different porosities. The optimized microstructures with 40, 50, and 70 % porosities are designed to satisfy the prescribed, numerically estimated cross-property parameters. The optimized material microstructures presented in Tables 2, 3 and 4 are similar to the microstructures given in (Guest and Prévost 2006; Chen et al. 2009; Chen et al. 2011; Guedes et al. 2003). The parameters for different cases are given in

Table 5. The results show how scaffold architecture affects tissue regeneration, since scaffolds can be fabricated to have different stiffness and permeability values for the same porosity.

It should also be noted that for the 3D microstructural design sometimes the final topologies will be similar at the first sight, but their detailed geometric features and fine shapes will be different. This indicates that the final properties of the optimized scaffold are determined not only by the topology but also by local geometrical shape and features of the internal surface, particularly for the design involving the boundary dependent conditions.

As illustrated in Tables 2, 3 and 4, different architectures of scaffold microstructures will give rise to different effective stiffness and permeability even under the same porosities. The porosity plays an important role in determining macroscopic properties of the scaffold as well. The range of stiffness able to be achieved is constrained by the bounds on the effective stiffness derived by Hashin and Shtrikman (Hashin and Shtrikman 1963). Furthermore, from the computational results, it can be seen that the arrangement of holes will effect on the effective permeability. Hollister (Hollister 2005) noted that for a specified scaffold design the effective permeability will decrease with the increase of material, and the effective permeability is only determined by the arrangement of holes. In addition, based on Eq. (8), the value of the effective permeability is dependent on the fluid velocities in the unit cell.

In the topology optimization design, we can also find that higher ratio of porosity for a microstructure indicates the removal of more base material, in order to facilitate a design with more internal pore connections to satisfy the tailored material properties. Under the no-slip condition, the length scales and the total areas of the flow channels have a large effect on the fluid velocities. This explains the phenomenon that Cases (d) and (h), and Cases (f) and (g) have similar topologies but different properties.

Since we have achieved a range of effective bulk moduli, the upper Hashin-Shtrikman bound (Hashin and Shtrikman 1963) for the bulk modulus will be used to validate the designed scaffold microstructure by using the proposed method. From Fig. 4, it can be seen that the bulk modulus of the optimized design are within the upper Hashin-Shtrikman bound. Sigmund (Sigmund 2002) also noted that the requirement to maintain mass transport might restrict the optimized microstructure from reaching the upper stiffness bounds. The optimization of stiffness only will lead to a closed unit cell architecture which may approach the upper Hashin-Shtrikman bound (Hashin and Shtrikman 1963). This also explains why the microstructure that is optimized with a fluid conductance constraint cannot reach the upper bounds. Guest (Guest and Prévost 2006) investigated the effect of a weighted combination of competing stiffness and flow terms in the objective function, and the numerical results (Guest and Prévost 2006)

Table 2 Optimized designs of scaffold architecture with the porosity 40 %

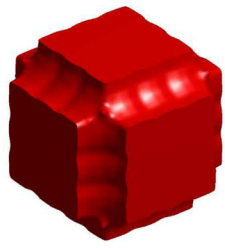
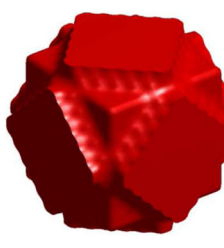
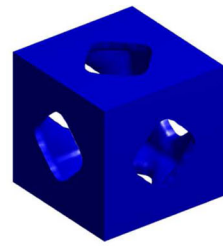
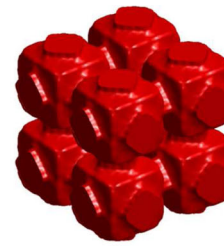
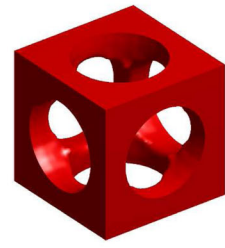
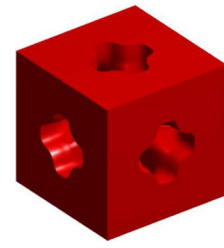
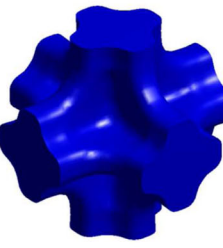
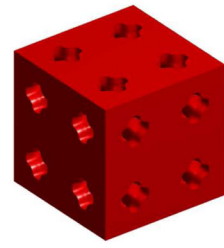
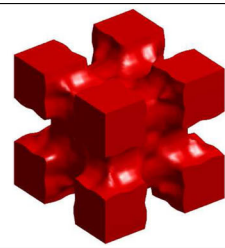
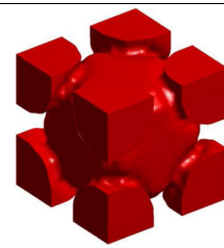
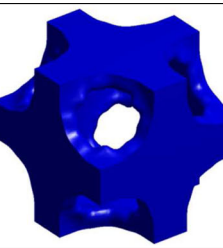
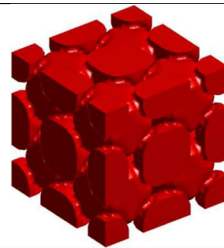
Case (a)	Initial guess (Solid phase)	Solid phase	Fluid phase	2×2×2 array		
						
Parameters of material properties	$\mathbf{C}^H = \begin{bmatrix} 0.6311 & 0.2099 & 0.2099 & 0 & 0 & 0 \\ 0.2099 & 0.6311 & 0.2099 & 0 & 0 & 0 \\ 0.2099 & 0.2099 & 0.6311 & 0 & 0 & 0 \\ 0 & 0 & 0 & 0.1698 & 0 & 0 \\ 0 & 0 & 0 & 0 & 0.1698 & 0 \\ 0 & 0 & 0 & 0 & 0 & 0.1698 \end{bmatrix}; \mathbf{K}^H = \begin{bmatrix} 0.0035 & 0 & 0 \\ 0 & 0.0035 & 0 \\ 0 & 0 & 0.0035 \end{bmatrix}$					
Case (b)	Initial guess (Solid phase)	Solid phase	Fluid phase	2×2×2 array		
						
Parameters of material properties	$\mathbf{C}^H = \begin{bmatrix} 0.5412 & 0.1621 & 0.1621 & 0 & 0 & 0 \\ 0.1621 & 0.5412 & 0.1621 & 0 & 0 & 0 \\ 0.1621 & 0.1621 & 0.5412 & 0 & 0 & 0 \\ 0 & 0 & 0 & 0.1513 & 0 & 0 \\ 0 & 0 & 0 & 0 & 0.1513 & 0 \\ 0 & 0 & 0 & 0 & 0 & 0.1513 \end{bmatrix}; \mathbf{K}^H = \begin{bmatrix} 0.3808 \times 10^{-3} & 0 & 0 \\ 0 & 0.3808 \times 10^{-3} & 0 \\ 0 & 0 & 0.3808 \times 10^{-3} \end{bmatrix}$					
Case (c)	Initial guess (Solid phase)	Solid phase	Fluid phase	2×2×2 array		
						
Parameters of material properties	$\mathbf{C}^H = \begin{bmatrix} 0.4924 & 0.1715 & 0.1715 & 0 & 0 & 0 \\ 0.1715 & 0.4924 & 0.1715 & 0 & 0 & 0 \\ 0.1715 & 0.1715 & 0.4924 & 0 & 0 & 0 \\ 0 & 0 & 0 & 0.1721 & 0 & 0 \\ 0 & 0 & 0 & 0 & 0.1721 & 0 \\ 0 & 0 & 0 & 0 & 0 & 0.1721 \end{bmatrix}; \mathbf{K}^H = \begin{bmatrix} 0.0024 & 0 & 0 \\ 0 & 0.0024 & 0 \\ 0 & 0 & 0.0024 \end{bmatrix}$					

Table 3 Optimized designs of scaffold architecture under the porosity 50 %

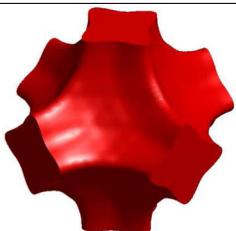
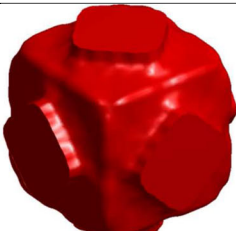
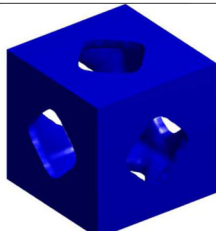
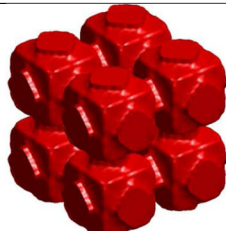
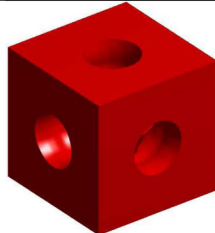
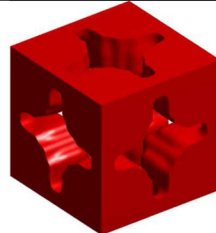
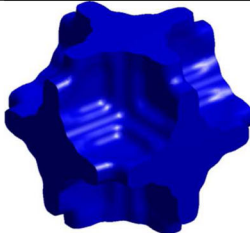
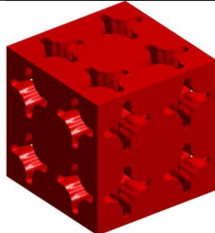
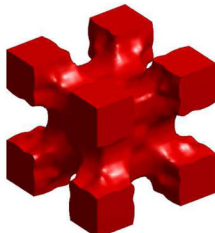
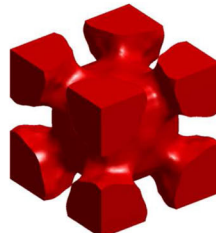
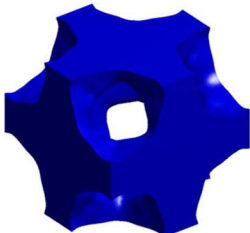
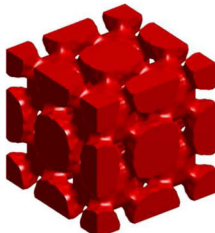
	Initial guess (Solid phase)	Solid phase	Fluid phase	2×2×2 array		
Case (d)						
Parameters of material properties	$C^H = \begin{bmatrix} 0.3645 & 0.0847 & 0.0847 & 0 & 0 & 0 \\ 0.0847 & 0.3645 & 0.0847 & 0 & 0 & 0 \\ 0.0847 & 0.0847 & 0.3645 & 0 & 0 & 0 \\ 0 & 0 & 0 & 0.0936 & 0 & 0 \\ 0 & 0 & 0 & 0 & 0.0936 & 0 \\ 0 & 0 & 0 & 0 & 0 & 0.0936 \end{bmatrix}; K^H = \begin{bmatrix} 0.007 & 0 & 0 \\ 0 & 0.007 & 0 \\ 0 & 0 & 0.007 \end{bmatrix}$					
Case (e)	Initial guess (Solid phase)	Solid phase	Fluid phase	2×2×2 array		
						
Parameters of material properties	$C^H = \begin{bmatrix} 0.1524 & 0.0164 & 0.0164 & 0 & 0 & 0 \\ 0.0164 & 0.1524 & 0.0164 & 0 & 0 & 0 \\ 0.0164 & 0.0164 & 0.1524 & 0 & 0 & 0 \\ 0 & 0 & 0 & 0.0392 & 0 & 0 \\ 0 & 0 & 0 & 0 & 0.0392 & 0 \\ 0 & 0 & 0 & 0 & 0 & 0.0392 \end{bmatrix}; K^H = \begin{bmatrix} 0.008 & 0 & 0 \\ 0 & 0.008 & 0 \\ 0 & 0 & 0.008 \end{bmatrix}$					
	Initial guess (Solid phase)	Solid phase	Fluid phase	2×2×2 array		
Case (f)						
Parameters of material properties	$C^H = \begin{bmatrix} 0.3701 & 0.1387 & 0.1387 & 0 & 0 & 0 \\ 0.1387 & 0.3701 & 0.1387 & 0 & 0 & 0 \\ 0.1387 & 0.1387 & 0.3701 & 0 & 0 & 0 \\ 0 & 0 & 0 & 0.1421 & 0 & 0 \\ 0 & 0 & 0 & 0 & 0.1421 & 0 \\ 0 & 0 & 0 & 0 & 0 & 0.1421 \end{bmatrix}; K^H = \begin{bmatrix} 0.0011 & 0 & 0 \\ 0 & 0.0011 & 0 \\ 0 & 0 & 0.0011 \end{bmatrix}$					

Table 4 Optimized designs of scaffold architecture under the porosity 70 %

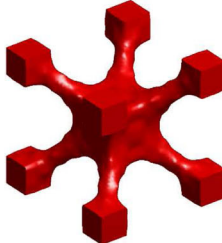
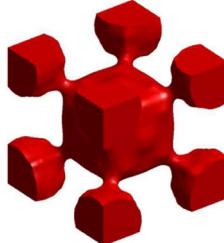
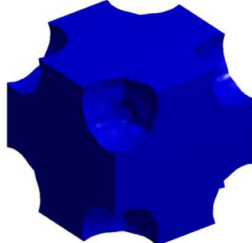
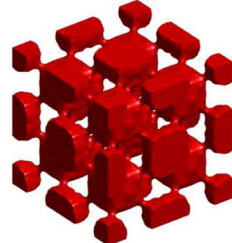
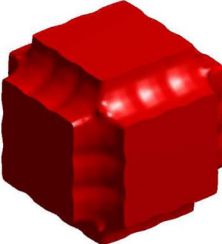
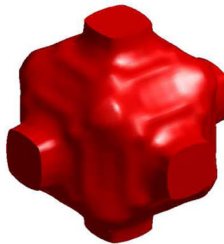
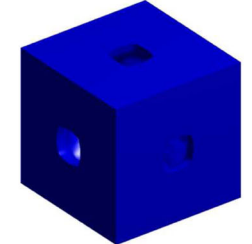
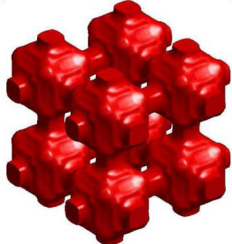
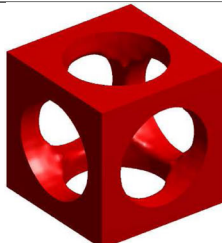
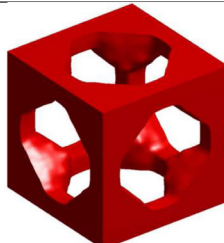
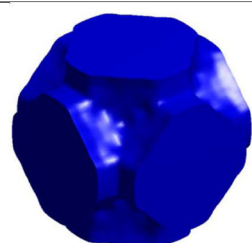
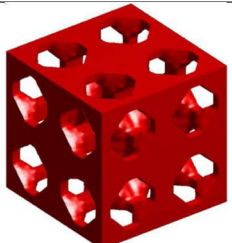
	Initial guess (Solid phase)	Solid phase	Fluid phase	2×2×2 array		
Case (g)						
Parameters of material properties	$C^H = \begin{bmatrix} 0.0979 & 0.0416 & 0.0416 & 0 & 0 & 0 \\ 0.0416 & 0.0979 & 0.0416 & 0 & 0 & 0 \\ 0.0416 & 0.0416 & 0.0979 & 0 & 0 & 0 \\ 0 & 0 & 0 & 0.0534 & 0 & 0 \\ 0 & 0 & 0 & 0 & 0.0534 & 0 \\ 0 & 0 & 0 & 0 & 0 & 0.0534 \end{bmatrix}; K^H = \begin{bmatrix} 4.422 \times 10^{-4} & 0 & 0 \\ 0 & 4.422 \times 10^{-4} & 0 \\ 0 & 0 & 4.422 \times 10^{-4} \end{bmatrix}$					
	Initial guess (Solid phase)	Solid phase	Fluid phase	2×2×2 array		
Case (h)						
Parameters of material properties	$C^H = \begin{bmatrix} 0.1650 & 0.0208 & 0.0208 & 0 & 0 & 0 \\ 0.0208 & 0.1650 & 0.0208 & 0 & 0 & 0 \\ 0.0208 & 0.0208 & 0.1650 & 0 & 0 & 0 \\ 0 & 0 & 0 & 0.0321 & 0 & 0 \\ 0 & 0 & 0 & 0 & 0.0321 & 0 \\ 0 & 0 & 0 & 0 & 0 & 0.0321 \end{bmatrix}; K^H = \begin{bmatrix} 0.0029 & 0 & 0 \\ 0 & 0.0029 & 0 \\ 0 & 0 & 0.0029 \end{bmatrix}$					
	Initial guess (Solid phase)	Solid phase	Fluid phase	2×2×2 array		
Case (i)						
Parameters of material properties	$C^H = \begin{bmatrix} 0.1960 & 0.0298 & 0.0298 & 0 & 0 & 0 \\ 0.0298 & 0.1960 & 0.0298 & 0 & 0 & 0 \\ 0.0298 & 0.0298 & 0.1960 & 0 & 0 & 0 \\ 0 & 0 & 0 & 0.0379 & 0 & 0 \\ 0 & 0 & 0 & 0 & 0.0379 & 0 \\ 0 & 0 & 0 & 0 & 0 & 0.0379 \end{bmatrix}; K^H = \begin{bmatrix} 2.269 \times 10^{-4} & 0 & 0 \\ 0 & 2.269 \times 10^{-4} & 0 \\ 0 & 0 & 2.269 \times 10^{-4} \end{bmatrix}$					

Table 5 Initial parameters and corresponding optimized results

Case	(ω_B, ω_k)	B^*	k^*	B^H	k^H
(a)	(1.00, 0.2)	0.2	0.005	0.3369	0.0035
(b)	(1.00, 0.1)	0.28	0.001	0.2849	0.0003808
(c)	(1.00, 0.2)	0.26	0.005	0.2786	0.0024
(d)	(1.00, 0.5)	0.18	0.005	0.18	0.007
(e)	(1.00, 0.5)	0.1	0.01	0.0693	0.008
(f)	(1.00, 0.02)	0.22	0.002	0.2167	0.0011
(g)	(1.00, 0.02)	0.06	0.001	0.0643	0.0004422
(h)	(1.00, 0.02)	0.07	0.005	0.0726	0.0029
(i)	(1.00, 0.02)	0.085	0.0005	0.0879	0.0002669

provided a reference for determining the weights in such multi-objective formulation. According to the specific requirements of scaffold design in our study, we found that the stiffness term takes priority in the optimized design.

The aim of this study is not to achieve maximum effective elastic properties or permeability with a constraint on porosity, but it is to generate new topologically optimized microstructures with desired properties for scaffolds whose properties can match those of natural bone tissue. There are potential applications for topologically optimized scaffolds with bio material in clinical research. The scaffolds to be used for different positions such as the trabecular bone and cartilage, they should have different properties (e.g. porosity and strength, stiffness, permeability). The optimized microstructure with 40 and 50 % porosities and high stiffness can be used for fracture fixation and fusion (Lin et al. 2004). For the spinal cage, it requires a scaffold with sufficient load bearing and limited displacement to ensure bone healing. The microstructures like Case (a) and Case (f), which almost reach the upper bound of the effective stiffness, can be considered in this application.

The microstructures with high porosity 70 % will be suitable for human trabecular bone such as distal femoral and iliac

crest (Goulet et al. 1994). Scaffold with low stiffness and low permeability are needed for cartilage tissue engineering applications (Kelly and Prendergast 2006). Such microstructures located within the interior of the cross property bounds and away from the upper limits, such as Case (g) and Case (i), can satisfy the requirements. Since the base material used in this study is artificial, it is difficult to compare the materials properties with those for real-world human tissues. Nevertheless, the topologically optimized microstructures with a range of cross properties can still provide a useful reference on how to design the scaffold architectures with controlled material properties.

Furthermore, to validate the numerical results, the properties of the optimized microstructure are compared with the properties of bi-optimal porous materials under cubic elastic and isotropic flow symmetries by Challis and et al. (Challis et al. 2012). In (Challis et al. 2012), the bi-optimal porous material design was obtained by setting equal weighting factors in the objective function ($\omega_B = \omega_k = 0.5$). To clarify the comparison, the computational results from (Challis et al. 2012) (the properties of porous material under different porosities, e.g. 10, 25, 50, 75 and 90 %) were plotted as a trend line, shown in Fig. 5. Comparing with the cases in (Challis et al. 2012), in this work the settings of weights for the objective function and the target properties are different. However, the results in (Challis et al. 2012) provided the computationally generated cross-property bounds, which can be regarded as references to the achieved effective properties in this work.

In Fig. 5, it can be seen that the properties obtained by the proposed method are reasonably around the bi-optimal cross-property lines. The designed microstructure under the given porosity 50 %, namely Case (d), shows a close value of the numerically estimated cross-property and a similar topology as given in (Challis et al. 2012). It is noted that the initial structures selected in these two studies are different. Due to the dependency of topologically optimized designs to the initial designs, the topologies of the final structures in these two

Fig. 4 Comparison of the achieved properties with the upper Hashin-Shtrikman bound (Chen et al. 2009)

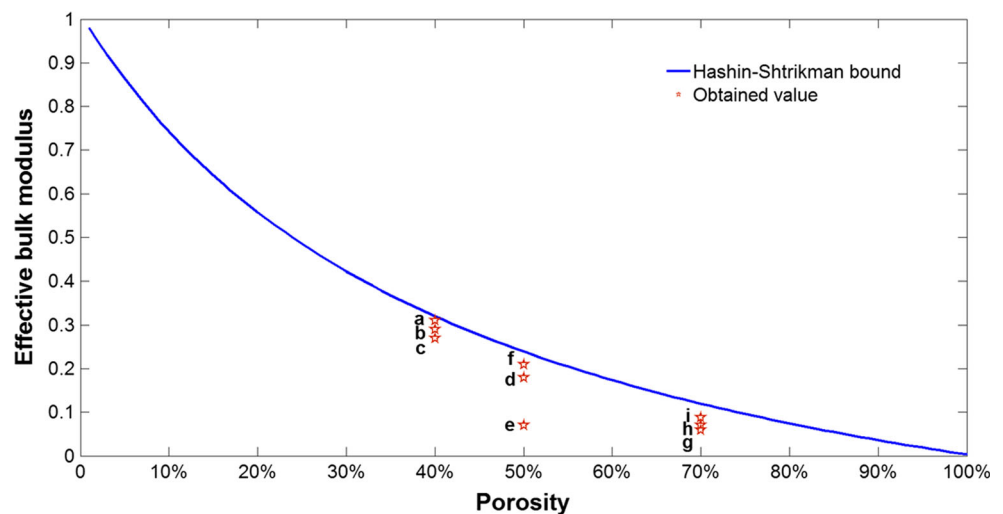
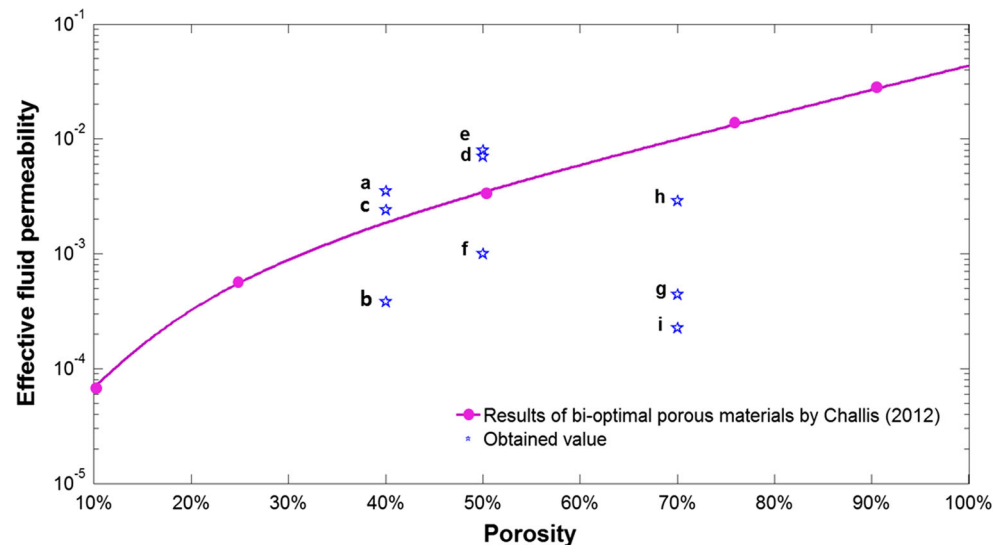


Fig. 5 Comparison of the achieved properties with the results of Challis (2012) (Challis et al. 2012)



works are different. Based on the resolutions in this study, it is not surprising to see that the topology optimization design problem under the same porosity may result in fluctuation in material properties. The variance of the effective stiffness can be caused by the different layouts of solid material, while the effective permeability are influenced by the size and shape of the 3D pores and pore connectivity. To meet the multifunctional needs of scaffold design, the goal of this study is to achieve a range of cross-properties by distributing a given amount of material with different layouts.

From the point of view of scaffold design in tissue engineering (Chen et al. 2011), tissue growth consideration is an important and challenging problem. In this paper, since the major concern is to develop a systematic design method for the creation of micro-structured mechanical architecture with prescribed material properties to assist scaffold design, we haven't considered the time-dependence of the tissue growth effect in the design of the scaffold. However, in our near future research, we will endeavor to develop a simplified method for design sensitivity analysis involving the time-dependent effect of tissue growth, so as to enable more practical bio engineering applications.

6 Conclusions

This paper has developed a systematic computational design method to generate micro-structured architectures using a multiphase level set method for 3D scaffolds in tissue engineering to achieve multifunctionality, e.g. mechanical stiffness, fluid porosity and permeability. The numerical homogenization method is integrated into the PLSM to optimize shape and topology of the microstructure. Several numerical examples have been applied to demonstrate the effectiveness of the proposed method. Moreover, the final microstructure is

geometrically characterized with smooth boundaries and distinct material interfaces, which may greatly facilitate fabrication of the topologically optimized scaffolds which normally have complex geometries and shapes. From the results, we can see that the proposed method can be used to generate a range of different scaffold architectures with various stiffness, porosity and permeability, to satisfy the multifunctionality of tissue engineering scaffolds. It is noted that the proposed method can be extended to more advanced design problems for scaffolds.

Acknowledgments This research is supported in part by the Australian Research Council (ARC)-Discovery Project (DP160102491, DP150102751), the National Natural Science Foundation of China (51575204), and the Science and Technology Support Program of Hubei Province of China (2015BHE026), as well as by the Open Research Foundation of State Key Lab. of Digital Manufacturing Equipment & Technology (DMETKF2015010), Huazhong University of Science & Technology, Wuhan, China.

References

- Allaire G, Jouve F, Toader A-M (2004) Structural optimization using sensitivity analysis and a level-set method. *J Comput Phys* 194: 363–393
- Bendsøe MP, Kikuchi N (1988) Generating optimal topologies in structural design using a homogenization method. *Comput Methods Appl Mech Eng* 71:197–224
- Bendsøe MP, Sigmund O (1999) Material interpolation schemes in topology optimization. *Arch Appl Mech* 69:635–654
- Bendsøe MP, Sigmund O (2003) *Topology optimization: theory, methods, and applications*. Springer, Berlin
- Boschetti F et al (2004) Biomechanical properties of human articular cartilage under compressive loads. *Biorheology* 41:159–166
- Challis VJ (2010) A discrete level-set topology optimization code written in Matlab. *Struct Multidiscip Optim* 41:453–464
- Challis VJ, Roberts AP, Wilkins AH (2008) Design of three dimensional isotropic microstructures for maximized stiffness and conductivity. *Int J Solids Struct* 45:4130–4146

- Challis VJ, Guest JK, Grotowski JF, Roberts AP (2012) Computationally generated cross-property bounds for stiffness and fluid permeability using topology optimization. *Int J Solids Struct* 49:3397–3408
- Chen YH, Zhou SW, Li Q (2009) Computational design for multifunctional microstructural composites. *Int J Mod Phys B* 23:1345–1351
- Chen YH, Zhou SW, Li Q (2011) Microstructure design of biodegradable scaffold and its effect on tissue regeneration. *Biomaterials* 32:5003–5014
- de Kruijf N, Zhou S, Li Q, Mai YW (2007) Topological design of structures and composite materials with multiobjectives. *Int J Solids Struct* 44:7092–7109
- Goulet RW et al (1994) The relationship between the structural and orthogonal compressive properties of trabecular bone. *J Biomech* 27: 375–389
- Guedes J, Kikuchi N (1990) Preprocessing and postprocessing for materials based on the homogenization method with adaptive finite element methods. *Comput Methods Appl Mech Eng* 83:143–198
- Guedes JM, Rodrigues HC, Bendsoe MP (2003) A material optimization model to approximate energy bounds for cellular materials under multiloading conditions. *Struct Multidiscip Optim* 25:446–452
- Guest JK, Prévost JH (2006) Optimizing multifunctional materials: design of microstructures for maximized stiffness and fluid permeability. *Int J Solids Struct* 43:7028–7047
- Guest JK, Prévost JH, Belytschko T (2004) Achieving minimum length scale in topology optimization using nodal design variables and projection functions. *Int J Numer Methods Eng* 61:238–254
- Hashin Z, Shtrikman S (1963) A variational approach to the theory of the elastic behaviour of multiphase materials. *J Mech Phys Solids* 11: 127–140
- Hollister SJ (2005) Porous scaffold design for tissue engineering. *Nat Mater* 4:518–524
- Hollister SJ, Maddox RD, Taboas JM (2002) Optimal design and fabrication of scaffolds to mimic tissue properties and satisfy biological constraints. *Biomaterials* 23:4095–4103
- Hughes TJR, Franca LP, Balestra M (1986) A new finite element formulation for computational fluid dynamics: V. Circumventing the babuška-brezzi condition. *Comput Methods Appl Mech Eng* 59: 85–99
- Kang Z, Wang Y (2011) Structural topology optimization based on non-local Shepard interpolation of density field. *Comput Methods Appl Mech Eng* 200:3515–3525
- Kang H, Lin CY, Hollister SJ (2010) Topology optimization of three dimensional tissue engineering scaffold architectures for prescribed bulk modulus and diffusivity. *Struct Multidiscip Optim* 42:633–644
- Kelly DJ, Prendergast PJ (2006) Prediction of the optimal mechanical properties for a scaffold used in osteochondral defect repair. *Tissue Eng* 12:2509–2519
- Lanza R, Langer R, Vacanti JP (2011) Principles of tissue engineering. Academic Press
- Lin CY, Kikuchi N, Hollister SJ (2004) A novel method for biomaterial scaffold internal architecture design to match bone elastic properties with desired porosity. *J Biomech* 37:623–636
- Luo Z, Wang MY, Wang S, Wei P (2008) A level set-based parameterization method for structural shape and topology optimization. *Int J Numer Methods Eng* 76:1–26
- Luo Z, Zhang N, Gao W, Ma H (2012a) Structural shape and topology optimization using a meshless Galerkin level set method. *Int J Numer Methods Eng* 90(3):369–389
- Luo Z, Zhang N, Ji J, Wu T (2012b) A meshfree level-set method for topological shape optimization of compliant multiphysics actuators. *Comput Methods Appl Mech Eng* 223–224:133–152
- Luo Z, Zhang N, Wang Y, Gao W (2013) Topology optimization of structures using meshless density variable approximants. *Int J Numer Methods Eng* 93:443–464
- Osher S, Fedkiw RP (2002) Level set methods and dynamic implicit surface. Springer, New York
- Osher S, Sethian JA (1988) Fronts propagating with curvature-dependent speed: algorithms based on Hamilton-Jacobi formulations. *J Comput Phys* 79:12–49
- Sethian JA (1999) Level set methods and fast marching methods: evolving interfaces in computational geometry, fluid mechanics, computer vision, and materials science. Cambridge University
- Sethian JA, Wiegmann A (2000) Structural boundary design via level set and immersed interface methods. *J Comput Phys* 163:489–528
- Sigmund O (2002) On the optimality of bone microstructure. Springer, Neverland
- Svanberg K (1987) The method of moving asymptotes—a new method for structural optimization. *Int J Numer Methods Eng* 24:359–373
- van Dijk NP, Maute K, Langelaar M, van Keulen F (2013) Level-set methods for structural topology optimization: a review. *Struct Multidiscip Optim* 48:437–472
- Wang MY, Wang X, Guo D (2003) A level set method for structural topology optimization. *Comput Methods Appl Mech Eng* 192: 227–246
- Wang YQ, Luo Z, Zhang N, Kang Z (2014) Topological shape optimization of microstructural metamaterials using a level set method. *Comput Mater Sci* 87:178–186
- Wang YQ, Luo Z, Kang Z, Zhang N (2015) A multi-material level set-based topology and shape optimization method. *Comput Methods Appl Mech Eng* 283:1570–1586
- Wendland H (2006) Computational aspects of radial basis function approximation. *Stud Comput Math* 12:231–256
- Xie YM, Steven GP (1993) A simple evolutionary procedure for structural optimization. *Comput Struct* 49:885–896
- Zhou M, Rozvany GIN (1991) The COC algorithm, Part II: topological, geometry and generalized shape optimization. *Comput Methods Appl Mech Eng* 89:197–224